Appendix A
Detailed Derivation of Impedance-Governed Generalized Snell's Law of Reflection (IGSL) in Acoustics

We mathematically derive the connection between the interface specific acoustic impedance (SAI) and the manipulation of wavefronts, which gives birth to the proposed impedance-governed generalized Snell's law of reflection (IGSL) as the design rule of SAI. In addition, we mathematically predict the double reflections and the situation when the ordinary reflection can be switched off.

We assume the time-harmonic factor in this appendix is $e^{-i\omega t}$, where ω is the circular frequency, and the coordinate system is that in Fig. A.1a. The incident acoustic pressure can be expressed as:

$$p_i(y, z, \omega) = p_{i0}(\omega) \exp[ik_0(y \sin\theta_i - z \cos\theta_i)], \tag{A.1}$$

where $k_0 = \omega/c_0$ is the wave number in free space, θ_i the incident angle and $p_{i0}(\omega)$ the amplitude. $Z_n(y, \omega) = p(y, 0, \omega)/[\mathbf{n} \cdot \mathbf{v}(y, 0, \omega)]$ as the specific acoustic impedance (SAI) [1] of a locally reacting boundary is laid at the interface, where $\mathbf{n}$ is the unit vector opposite to z direction and $\mathbf{v}$ is the acoustic velocity. The boundary condition of this problem can be paraphrased as [2]:

$$\frac{\partial}{\partial z} p(y, 0, \omega) + ik_0 \beta(y, \omega) p(y, 0, \omega) = 0, \tag{A.2}$$

where $\beta(y, \omega) = \rho_0 c_0 / Z_n(y, \omega)$ (ρ_0 and c_0 being the given density and sound speed respectively in the upper space) is the normalized acoustical admittance of the locally reacting surface.

We expand β to be $\beta(y, \omega) = \tilde{\beta}(y, \omega) + \beta_0(\omega)$, where β_0 is a real constant. The ordinary reflection is expressed as:

$$p_{ro}(y, z, \omega) = p_{i0}(\omega) R(\theta_i, \beta_0) \exp[ik_0(y \sin\theta_{ro} + z \cos\theta_{ro})], \tag{A.3}$$

where R is the reflection coefficient and θ_{ro} the angle of p_{ro}. Because p_{ro} observes the usual Snell's law, $\theta_{ro} = \theta_i$. In order to find the expression of R, we introduce the constant SAI:

J. Zhao, *Manipulation of Sound Properties by Acoustic Metasurface and Metastructure*, Springer Theses, DOI 10.1007/978-981-10-2125-1

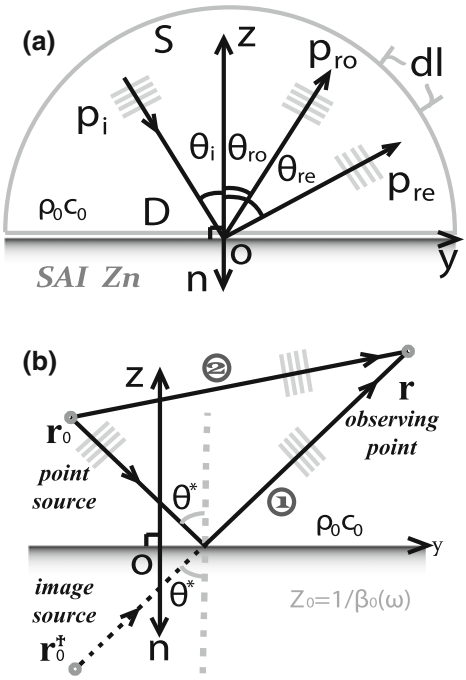

Fig. A.1 **a** Illustration for some notations. The *gray curve* indicates the contour of the Green's integral. S is the semicircular contour; D is the flat one along the surface. p_i, p_{ro} and p_{re} denote the incidence, the ordinary reflection, and the extraordinary reflection, respectively. $\mathbf{n}$ is the unit vector opposite to z direction. Z_n is set for the flat interface ($z = 0$). **b** Schematic diagram for the effective paths of acoustic radiation. The introduced θ^* can be interpreted as the effective incident angle. $\mathbf{r}$, $\mathbf{r}_0$, and $\mathbf{r}_0^\dagger$ are the location vectors for the point source, the image source and the observer, respectively

$$Z_0(\omega) = \frac{\rho_0 c_0}{\beta_0(\omega)} = \frac{p_i(y,0,\omega) + p_{ro}(y,0,\omega)}{\mathbf{n}\cdot\mathbf{v}_i(y,0,\omega) + \mathbf{n}\cdot\mathbf{v}_{ro}(y,0,\omega)}, \tag{A.4}$$

where $\mathbf{n}$ is the normal vector indicated in Fig. A.1a, $\mathbf{v}_i$ and $\mathbf{v}_{ro}$ the acoustic velocities of p_i and p_{ro}. Substituting Eqs. (A.1) and (A.3) into Eq. (A.4) and applying Euler equation $\rho_0 \frac{\partial}{\partial t}\mathbf{v} = -\nabla p$, we obtain:

$$R(\theta_i, \beta_0) = \frac{\cos\theta_i - \beta_0(\omega)}{\cos\theta_i + \beta_0(\omega)}. \tag{A.5}$$

In Fig. A.1a, the total acoustic field can be written in the integral form:

$$\begin{aligned} p(y,z,\omega) = \oint_{S+D} dl[&G(y,z,\omega;y_0,z_0)\frac{\partial}{\partial n_0}p(y_0,z_0,\omega) \\ &- p(y_0,z_0,\omega)\frac{\partial}{\partial n_0}G(y,z,\omega;y_0,z_0)], \end{aligned} \tag{A.6}$$

where $dl(y_0, z_0)$ is the infinitesimal segment along the integral contour, $\mathbf{n}_0 = \mathbf{n}(y_0, z_0)$ and $G(y, z, \omega; y_0, z_0)$ is the Green's function corresponding to the following partial differential problem:

$$\begin{aligned}&\nabla^2 G + {k_0}^2 G = -\delta(y - y_0)\delta(z - z_0), z > 0\\&[\tfrac{\partial}{\partial z_0} G + ik_0\beta_0(\omega)G]\Big|_{z_0=0} = 0\end{aligned}. \tag{A.7}$$

When the radius of the semicircular contour S approaches ∞, we can regard the contour integral along S is mainly contributed by p_i and p_{ro}. Therefore Eq. (A.6) changes to be:

$$\begin{aligned}p(y, z, \omega) =& p_i(y, z, \omega) + p_{ro}(y, z, \omega)\\&- \int_{-\infty}^{\infty} dy_0[G\frac{\partial}{\partial z_0} p(y_0, z_0, \omega) - p(y_0, z_0, \omega)\frac{\partial}{\partial z_0} G].\end{aligned} \tag{A.8}$$

We can simplify Eq. (A.8) by substituting Eqs. (A.7) and (A.2) into it. By defining the last part in Eq. (A.9) as the extraordinary reflection $p_{re}(y, z, \omega)$, which is the unique extra component beyond p_{ro}, we obtain

$$p_{re}(y, z, \omega) = ik_0 \int_{-\infty}^{\infty} \tilde{\beta}(y_0, \omega) p(y_0, 0, \omega) G(y, z, \omega; y_0, 0) dy_0. \tag{A.9}$$

The explicit solution of $G(y, z, \omega; y_0, z_0)$ in Eq. (A.7) is

$$\begin{aligned}G =& \frac{i}{4} H_0^{(1)}(k_0 |\mathbf{r} - \mathbf{r}_0|)\\&+ \frac{i}{4\pi} \int_{-\infty}^{\infty} \frac{1}{k_z} \frac{k_z - \omega\beta_0/c_0}{k_z + \omega\beta_0/c_0} \exp[ik_z(z + z_0) + ik_y(y - y_0)] dk_y,\end{aligned} \tag{A.10}$$

where $\mathbf{r} = (y, z)$, $\mathbf{r}_0 = (y, z)$, and ${k_0}^2 = {k_y}^2 + {k_z}^2$. When $\mathbf{r}$ is away from the surface D, $k_z \approx k_0 \cos\theta^*$ holds, where θ^* is introduced as a constant. Via this approximation and another definition $\mathbf{r}_0^\dagger = (y_0, -z_0)$, it turns out that [3]

$$\cos\theta^* \approx \frac{z - (-z_0)}{\left|\mathbf{r} - \mathbf{r}_0^\dagger\right|} \approx constant. \tag{A.11}$$

Through Eq. (A.11), it can be obtained that

$$\frac{k_z - \omega\beta_0/c_0}{k_z + \omega\beta_0/c_0} \approx \frac{\cos\theta^* - \beta_0(\omega)}{\cos\theta^* + \beta_0(\omega)} \approx constant \approx R(\theta^*, \beta_0). \tag{A.12}$$

Applying Eq. (A.12) into Eq. (A.10) and using the formula of the cylindrical wave expansion in terms of plane waves, we approach a neat form of the Green's function:

$$G(y, z, \omega; y_0, z_0) \approx \frac{i}{4} H_0^{(1)}(k_0 |\mathbf{r} - \mathbf{r}_0|) + R(\theta^*, \beta_0) \frac{i}{4} H_0^{(1)}(k_0 \left|\mathbf{r} - \mathbf{r}_0^\dagger\right|), \tag{A.13}$$

where $H_0^{(1)}(\cdot)$ the Hankel function of the first kind [4].

From the physical insight into Eq. (A.13), the first part of G is the direct contribution of the point source to the observer through path 2 in Fig. A.1b. The second part is the product of the Green's function excited by the image source and the reflection coefficient R, denoting p_{ro}. According to our interpretation, Fig. A.1b illustrates path 1 and path 2, visualized as p_{ro} and p_{re} respectively [3]. Due to the expression of R, we figure out that θ^* is the effective incident angle regarding to Fig. A.1b. Furthermore, it is reasonable to say that the major contribution of the integral in Eq. (A.10) is attributed to the vicinity of θ^*, in which way R can be regarded as a constant and put outside the integral.

By far-field approximation, we are able to get these expansions:

$$\begin{aligned} \mathbf{r}\cdot\mathbf{r}_0 &= r(y_0\sin\theta + z_0\cos\theta) \\ \mathbf{r}\cdot\mathbf{r}_0^{\dagger} &= r(y_0\sin\theta - z_0\cos\theta) \\ H_0^{(1)}(x)\Big|_{x\to\infty} &\approx \sqrt{\tfrac{2}{\pi x}}e^{i(x-\frac{\pi}{4})} \end{aligned}, \tag{A.14}$$

where r is the length of $\mathbf{r}$; $\sin\theta = y/r$; $\cos\theta = z/r$. Substituting Eqs. (A.14) and (A.5) into Eq. (A.13), we obtain:

$$G(y,z,\omega;y_0,0) \approx i\sqrt{\frac{1}{2\pi k_0 r}}e^{i(k_0 r-\frac{\pi}{4})}e^{-ik_0 y_0\sin\theta}\frac{\cos\theta^*}{\cos\theta^*+\beta_0(\omega)}. \tag{A.15}$$

After substituting Eq. (A.15) into Eq. (A.9), the extraordinary reflection becomes:

$$p_{re} \approx -\sqrt{\frac{k_0}{2\pi r}}e^{i(k_0 r-\frac{\pi}{4})}\frac{\cos\theta^*}{\cos\theta^*+\beta_0(\omega)}\int_{-\infty}^{\infty}\tilde{\beta}(y_0,\omega)p(y_0,0,\omega)e^{-ik_0 y_0\sin\theta_{re}}dy_0. \tag{A.16}$$

Further, after applying Born approximation to Eq. (A.16) and expanding it by Eqs. (A.1) and (A.3), p_{re} becomes:

$$\begin{aligned} p_{re} \approx &-\sqrt{\frac{2k_0}{\pi r}}\times\frac{p_{i0}(\omega)\exp[i(k_0 r-\frac{\pi}{4})]\cos\theta^*\cos\theta_i}{[\cos\theta^*+\beta_0(\omega)][\cos\theta_i+\beta_0(\omega)]} \\ &\times\int_{-\infty}^{\infty}\tilde{\beta}(y_0,\omega)e^{ik_0 y_0(\sin\theta_i-\sin\theta_{re})}dy_0. \end{aligned} \tag{A.17}$$

Now we consider our proposed SAI:

$$Z_n(y,\omega) = A\left[1 - i\tan\frac{\psi(y)}{2}\right];\ \beta_0(\omega) = \frac{\rho_0 c_0}{2A}. \tag{A.18}$$

After substituting Eq. (A.18) into Eqs. (A.3) and (A.17), we obtain the ordinary reflection and the extra reflection: extraordinary reflection:

$$p_{ro} \propto \frac{2A\cos\theta_i - \rho_0 c_0}{2A\cos\theta_i + \rho_0 c_0} \exp[ik_0(y\sin\theta_{ro} + z\cos\theta_{ro})], \tag{A.19}$$

$$p_{re} \propto \int_{-\infty}^{\infty} e^{i\psi(y)} e^{ik_0 y(\sin\theta_i - \sin\theta_{re})} dy. \tag{A.20}$$

Here note that in our case we are able to create *double reflections* by means of SAI inhomogeneity.

Equation (A.20) is a Dirac Delta if we consider $\psi(y)$ to be a linear term as the first order approximation. Or else, we know that the integral in Eq. (A.20) will reach the maximum by imposing the stationary phase approximation, i.e.,

$$\sin\theta_{re} - \sin\theta_i = \frac{1}{k_0}\frac{d\psi(y)}{dy}. \tag{A.21}$$

Although Eq. (A.21) corresponds to the form of the generalized Snell's law of reflection (GSL) [5], the variables in the two situations are different. Starting from Eq. (A.18) and ending up with Eq. (A.21), we provide the insight between our designed SAI and the direction of p_{re}, without considering the phase in terms of wave propagation. We name Eq. (A.21) as IGSL in acoustics, as the design principle of the SAI equation (A.18).

According to Eq. (A.19), if $A = (\rho_0 c_0)/(2\cos\theta_i)$, we can switch off p_{ro}. Therefore Eq. (A.18) becomes

$$Z_n(y,\omega) = \frac{\rho_0 c_0}{2\cos\theta_i}\left[1 - i\tan\frac{\psi(y)}{2}\right]. \tag{A.22}$$

References

1. D.T. Blackstock, *Fundamentals of Physical Acoustics* (Wiley, New York, 2000)
2. M.A. Nobile, S.I. Hayek, Acoustic propagation over an impedance plane. J. Acoust. Soc. Am. **78**(4), 1325–1336 (1985) nces
4. C. Chien, W. Soroka, Sound propagation along an impedance plane. J. Sound Vib. **43**(1), 9–20 (1975)
5. N. Yu, P. Genevet, M.A. Kats, F. Aieta, J.-P. Tetienne, F. Capasso, Z. Gaburro, Light propagation with phase discontinuities: generalized laws of reflection and refraction. Science **334**(6054), 333–337 (2011)

Appendix B
Distinction of IGSL in Acoustics

The same appearance of the impedance-governed generalized Snell's law of reflection (IGSL) and the generalized Snell's law of reflection (GSL) may cause the false impression that our IGSL is the same as GSL. Actually their mechanisms are totally distinct.

In terms of phase inhomogeneity, the anomalous reflection p_{ra} actually corresponds to the situation when the ordinary reflection p_{ro} is steered toward a "wrong" direction governed by GSL [1], illustrated in Fig. B.1a. There is only one single direction of reflection all the while. On the contrary in terms of SAI inhomogeneity, it is found that IGSL cannot alter p_{ro} by an SAI interface, but can "turn off" p_{ro} so as to provide insight into the engineering of special wavefronts by SAI interface, illustrated in Fig. B.1b. Moreover, the extraordinary reflection p_{re} governed by IGSL is an additionally unique component in acoustics, which can be "geared" along arbitrary directions, simultaneously with vanishing p_{ro}. Therefore, our proposed IGSL opens up rich effects and unprecedented applications in the community of acoustics. Additionally, GSL can even be considered as one subset of IGSL, when p_{ro} is turned off. In order to stress the irrelevance between IGSL and GSL again, we list the differences:

1. GSL is initiated in electromagnetism with electric properties; IGSL is initiated in acoustics with mechanical properties.
2. GSL is derived from Fermat Principle, i.e., the conservation of the wave number along an interface; IGSL is derived from Green's function. The fundamental physics is distinguished.
3. The variable of GSL is phase inhomogeneity; the variable of IGSL is impedance inhomogeneity. The methods are independent.
4. GSL will only generate single reflection; IGSL not only can generate single reflection, but also can generate double reflections.
5. GSL acts upon p_{ro}; IGSL acts upon p_{re}.
6. In GSL, the anomalous reflection corresponds to the situation where p_{ro} is tweaked toward a different direction governed by GSL; in acoustics, IGSL cannot alter p_{ro} by SAI interfaces, but is capable of "turning on" or "turning off" p_{ro}.

J. Zhao, *Manipulation of Sound Properties by Acoustic Metasurface and Metastructure*, Springer Theses, DOI 10.1007/978-981-10-2125-1

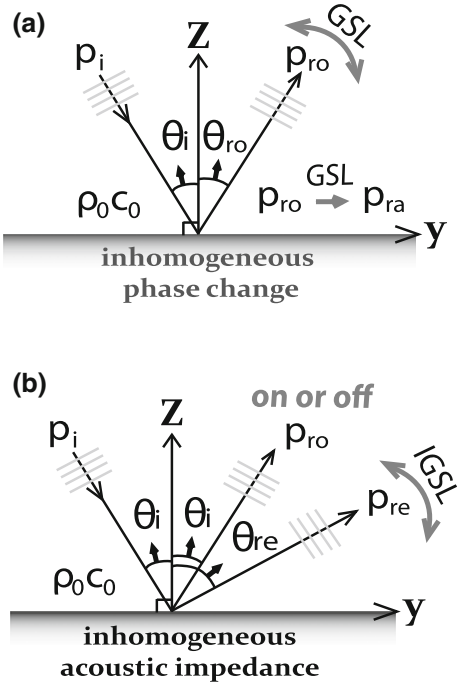

Fig. B.1 **a** For a flat interface with an inhomogeneous phase change, the angle of p_{ro}, i.e., θ_{ro}, is tweaked in a fashion of GSL. The manipulated "ordinary reflection" is called to be the anomalous reflection p_{ra} in terms of GSL [1]. **b** For a flat interface with an inhomogeneous SAI, $\theta_{ro} = \theta_i$ without influence, while p_{re} occurs simultaneously and θ_{re} is controlled by IGSL, implying double reflections. If SAI is properly controlled, p_{ro} can be switched off

Reference

1. N. Yu, P. Genevet, M.A. Kats, F. Aieta, J.-P. Tetienne, F. Capasso, Z. Gaburro, Light propagation with phase discontinuities: generalized laws of reflection and refraction. Science **334**(6054), 333–337 (2011)

Appendix C
Parameters of Metasurface Piezoelectric Transducer

C.1 Parameters of Lead Zirconate Titanate PZT-5H

The density of PZT-5H is 7500 kg/m^3. See Tables C.1, C.2 and C.3.

Table C.1 Symmetric elasticity matrix (Pa)

1.27×10^{11}	8.02×10^{10}	8.47×10^{10}	0	0	0
0	1.27×10^{11}	8.47×10^{10}	0	0	0
0	0	1.17×10^{11}	0	0	0
0	0	0	2.30×10^{10}	0	0
0	0	0	0	2.30×10^{10}	0
0	0	0	0	0	2.35×10^{10}

Table C.2 Relative permittivity ε_{Sr}

1704.4	0	0
0	1704.4	0
0	0	1433.6

Table C.3 Coupling matrix e (C/m^2)

0	0	0	0	17.0345	0
0	0	0	17.0345	0	0
−6.6228	−6.6228	23.2403	0	0	0

J. Zhao, *Manipulation of Sound Properties by Acoustic Metasurface and Metastructure*, Springer Theses, DOI 10.1007/978-981-10-2125-1

C.2 Optimized Configuration of Ring Pattern

See Tables C.4, C.5 and C.6

Table C.4 Configuration of 30 rings to generate a focal needle (mm)

r1	2.95	r7	36.68	r13	71.28	r19	102.62	r25	137.42
rr1	7.07	rr7	40.79	rr13	75.39	rr19	106.74	rr25	141.54
r2	8.19	r8	43.37	r14	76.35	r20	109.67	r26	143.69
rr2	12.31	rr8	47.49	rr14	80.47	rr20	113.78	rr26	147.81
r3	13.27	r9	49.20	r15	81.39	r21	114.91	r27	150.20
rr3	17.39	rr9	53.32	rr15	85.51	rr21	119.02	rr27	154.32
r4	19.32	r10	56.02	r16	86.77	r22	120.05	r28	156.36
rr4	23.44	rr10	60.13	rr16	90.89	rr22	124.17	rr28	160.48
r5	24.66	r11	60.79	r17	92.76	r23	126.30	r29	161.12
rr5	28.78	rr11	64.90	rr17	96.88	rr23	130.41	rr29	165.23
r6	30.33	r12	66.25	r18	97.84	r24	131.53	r30	167.04
rr6	34.45	rr12	70.36	rr18	101.95	rr24	135.65	rr30	171.16

Table C.5 Configuration of 28 rings to generate multiple foci (mm)

r1	6.86	r8	49.05	r15	107.70	r22	171.84
rr1	10.98	rr8	53.17	rr15	111.82	rr22	175.96
r2	13.03	r9	55.22	r16	116.96	r23	183.50
rr2	17.15	rr9	59.34	rr16	121.08	rr23	187.62
r3	17.49	r10	63.80	r17	123.82	r24	194.14
rr3	25.73	rr10	67.92	rr17	127.94	rr24	198.26
r4	27.44	r11	72.37	r18	131.71	r25	201.34
rr4	31.56	rr11	76.49	rr18	135.83	rr25	205.46
r5	32.58	r12	79.92	r19	143.03	r26	216.09
rr5	36.70	rr12	84.04	rr19	147.15	rr26	220.21
r6	37.04	r13	86.78	r20	156.06	r27	230.49
rr6	41.16	rr13	90.90	rr20	160.18	rr27	238.73
r7	42.53	r14	95.69	r21	164.64	r28	244.90
rr7	46.65	rr14	99.81	rr21	168.76	rr28	249.02

Table C.6 Configuration of 19 rings to generate super-oscillatory super resolution (mm)

r1	5.33	r6	46.56	r11	91.79	r16	136.87
rr1	9.61	rr6	50.84	rr11	96.08	rr16	141.15
r2	11.77	r7	55.50	r12	99.74	r17	145.58
rr2	16.05	rr7	59.79	rr12	104.03	rr17	149.87
r3	19.97	r8	64.13	r13	111.33	r18	151.41
rr3	24.26	rr8	68.42	rr13	115.61	rr18	155.69
r4	29.33	r9	72.18	r14	118.42	r19	159.96
rr4	33.62	rr9	76.47	rr14	122.71	rr19	167.56
r5	39.35	r10	81.53	r15	128.72		
rr5	43.64	rr10	85.82	rr15	133.01		

Appendix D
Details of the Simulation for Internal Waves

We conduct direct numerical simulations for tidal flow over synthetic random topography. The computational domain of width 10 km has periodic boundary conditions on the sides and a no-slip boundary condition on the random bottom topography. Wave reflection from the top boundary of the domain is avoided by adding a Rayleigh damping force that gradually increases upward. The damping force starts from a height of 5 km and goes up to the domain top of 15.5 km height; the approximately 3×10^6 control volumes have unstructured grids.

The simulations use the CDP 2.4 code, which implements a fractional-step time-marching scheme [1]. This code with disabled sub-grid modeling and an addition of buoyancy forces has been used and validated in previous studies of IW generation by tidal flow in stratified fluids [2–4]. Tidal flow is produced by adding a horizontal force, $F(t) = \rho_0 U_0 \omega cos(\omega t)$, to the momentum equation. We use $U_0 = 0.14$ cm/s, resulting in a tidal excursion close to $U_0/\omega = 10$ m. The small excursion relative to the autocorrelation widths of the topographies is chosen to avoid overturning and turbulence, since the interest here is in the radiation. The viscosity, $\nu = 0.01\,\mathrm{m}^2/\mathrm{s}$, is four orders larger than that of water to reduce the simulation cost (sparser grids are needed for higher ν); however, the large viscosity has a negligible effect on tidal conversion in the regime of laminar flow [3]. The salt diffusivity κ is $2 \times 10^{-5}\,\mathrm{m}^2/\mathrm{s}$, which gives negligible diffusion for the large Schmidt number, $\nu/\kappa = 500$. Each simulation has 2000 time steps per period and extends for 20 tidal periods to ensure a steady state. The convergence is tested by doubling the spatial and temporal resolution; this changes the computed IW power by less than 3 %.

The radiated IW power is calculated from the horizontal integral of the vertical energy flux averaged over a tidal period, $\Phi_z(x, z) \equiv \langle p' \mathbf{v}' \rangle_t$ at $z = z_{top}$, where z_{top} is the maximum topographic height, p' is the wave pressure, and $\mathbf{v}'$ is the wave velocity, given by $\mathbf{v}'(x, z, t) = \mathbf{v}(x, z, t) - \mathbf{v}_{baro}(z, t)$, where $\mathbf{v}(x, z, t)$ is the fluid velocity and $\mathbf{v}_{baro}(z, t)$ is the barotropic velocity, which in our simulations is approximated by $U_0 sin(\omega t)$ because our domain height is much taller than the topographic height (thus the flow acceleration over the topography is negligible). An example of the time-averaged energy flux field $\Phi_z(x, z)$ from our simulations is shown in Fig. 6.1a.

J. Zhao, *Manipulation of Sound Properties by Acoustic Metasurface and Metastructure*, Springer Theses, DOI 10.1007/978-981-10-2125-1

References

1. F. Ham, G. Iaccarino, Annual Research Briefs, Center for Turbulence Research. Stanford, CA, pp. 3–14 (2004)
2. B. King, H. Zhang, H.L. Swinney, Tidal flow over three-dimensional topography in a stratified fluid. Phys. Fluids **21**(11), 116601 (2009)
3. A. Dettner, H.L. Swinney, M. Paoletti, Internal wave and boundary current generation by tidal flow over topography. Phys. Fluids **25**(11), 116601 (2013)
4. L. Zhang, H.L. Swinney, Virtual seafloor reduces internal wave generation by tidal flow. Phys. Rev. Lett. **112**(10), 104502 (2014)